

Cite this: *J. Mater. Chem. A*, 2021, 9, 11802

$K_{1.5}VOPO_4F_{0.5}$: a novel high-power and high-voltage cathode for rechargeable K-ion batteries†

Hyunyoung Park,^a Wonseok Ko,^a Yongseok Lee,^a Jungmin Kang,^a Jinho Ahn,^a Jung-Keun Yoo^{*b} and Jongsoo Kim^{†*a}

High-performance cathode materials for K-ion batteries require large K^+ diffusion pathways and numerous K^+ sites in the stable crystal structure. Herein, we investigate $K_{1.5}VOPO_4F_{0.5}$ composed of three-dimensionally interconnected $[V_2O_{10}F]$ bi-octahedra and $[PO_4]$ tetrahedra as a promising cathode material for K-ion batteries using a combined computational and experimental approach. First-principles calculation results reveal that K^+ ions can be readily diffused along large two-dimensional pathways in the $K_{1.5}VOPO_4F_{0.5}$ structure and that numerous K^+ ions can be reversibly de/intercalated in the available voltage range, demonstrating the potential of $K_{1.5}VOPO_4F_{0.5}$ to deliver outstanding electrochemical performance in a K-ion battery system. At a current rate of $C/20$ ($1C = 116 \text{ mA g}^{-1}$), the specific capacity of $K_{1.5}VOPO_4F_{0.5}$ is retained up to $\sim 116 \text{ mA h g}^{-1}$ with a high average operation voltage of $\sim 3.8 \text{ V}$ (vs. K^+/K), corresponding to reversible de/intercalation of $\sim 1 \text{ mol } K^+$ in the structure. Even at $5C$, $K_{1.5}VOPO_4F_{0.5}$ delivers $\sim 79\%$ of the capacity measured at $C/20$, indicating its excellent power-capability despite the large ionic size of K^+ . Moreover, $K_{1.5}VOPO_4F_{0.5}$ delivers excellent cycle performance, with $\sim 86\%$ retention of the initial capacity after 300 cycles at $1C$ and a high coulombic efficiency of over 99%. Combined studies using *ex situ* XANES analyses and first-principles calculation indicate occurrence of V^{4+}/V^{5+} redox reaction of $K_{1.5}VOPO_4F_{0.5}$ for its high operation voltage. We believe that our findings will provide highly useful guidance for the discovery of high-performance electrode materials for rechargeable batteries.

Received 17th March 2021
Accepted 24th April 2021

DOI: 10.1039/d1ta02247d

rsc.li/materials-a

Introduction

To overcome the global environmental issues stemming from the use of fossil fuels, considerable efforts are needed in the development of not only renewable energy sources but also efficient energy storage systems (ESSs).¹ Lithium-ion batteries (LIBs) have received great attention as one of the most promising ESSs because of their high energy densities and long lifetime.^{2–4} Thanks to these advantages, the initial application of LIBs in small electronic devices has now expanded to mid- to large-sized ESSs such as electric vehicles (EVs).^{5–7} However, given the limited reserve of lithium resources and their localized distribution, it may be difficult to satisfy the explosively increasing demands for LIBs in the near future.⁸ Thus, many researchers have focused on the development of low-cost ESSs as alternatives to LIBs for grid-scale application.

Potassium-ion batteries (KIBs) are considered promising alternatives to LIBs because of the earth-abundant reserves of potassium sources and lower redox potential of K/K^+ (-2.93 V vs. the standard hydrogen electrode (SHE)) than Na/Na^+ (-2.71 V vs. SHE) and Mg/Mg^{2+} (-2.27 V vs. SHE).^{9,10} Moreover, the monovalent-ion-based de/intercalation chemistry in the KIB system is comparable to that in the LIB system, which suggests that KIBs could be more smoothly applied to the established LIB system than other ESSs.¹¹ However, the larger ionic size of K^+ ($\sim 1.38 \text{ \AA}$) compared with that of Li^+ ($\sim 0.76 \text{ \AA}$) leads to not only more sluggish ion diffusion but also more severe structural change during de/intercalation. To overcome these issues, KIB cathode materials must possess large K^+ diffusion pathways with numerous K sites in the stable crystal structure. Layered-type materials have received great attention as promising cathode materials for KIBs owing to their large theoretical gravimetric capacities relative to those of other KIB cathode materials.¹² Nevertheless, realization of the theoretical properties of layered-type cathode materials for KIBs in the available operation voltage ranges is difficult because of the severe structural changes resulting from de/intercalation of the large K^+ ions.^{13,14} However, for polyanionic compounds composed of three-dimensionally interconnected MO_6 octahedra (M : Fe, Mn, V, etc.) and XO_4 tetrahedra (X = P, S, Si, etc.), their rigid

^aDepartment of Energy Science, Sungkyunkwan University, Suwon, 16419, Republic of Korea. E-mail: jongsookim@skku.edu

^bCarbon Composites Department, Composites Research Division, Korea Institute of Materials Science (KIMS), 797 Changwondaero, Changwon, 51508, Republic of Korea. E-mail: yoojk@kims.re.kr

† Electronic supplementary information (ESI) available: Supplementary figures and tables. See DOI: 10.1039/d1ta02247d

crystal frameworks can effectively suppress the severe structural degradation resulting from de/intercalation of large K^+ ions, implying the high possibility of realizing the theoretical properties of polyanionic compounds in the KIB system.¹⁵ Moreover, the inductive effect derived from XO_4 tetrahedra with strong electronegativity enables high redox potentials of transition metal ions, resulting in large energy densities of polyanionic compounds despite their relatively low theoretical gravimetric capacities.^{16,17}

In this work, we explored a novel polyanionic compound, $K_{1.5}VOPO_4F_{0.5}$, as a promising cathode material for KIBs. The co-existence of $(PO_4)^{3-}$ and F^- with the highest electronegativity in the structure enables the high operation voltages of $K_{1.5}VOPO_4F_{0.5}$ in the KIB system.^{18–21} Through structural analyses, including Rietveld refinement and bond-valence energy landscape (BVEL) analysis based on X-ray diffraction (XRD), we demonstrate that the three-dimensional crystal framework of $K_{1.5}VOPO_4F_{0.5}$ contains large two-dimensional K^+ diffusion pathways and numerous K sites, which implies the possibility of facile K^+ de/intercalation in $K_{1.5}VOPO_4F_{0.5}$ without severe structural degradation as well as a large theoretical capacity. The combined studies using first-principles calculation and electrochemical tests indicate that $K_{1.5}VOPO_4F_{0.5}$ delivers a specific capacity of $\sim 116 \text{ mA h g}^{-1}$ with a high average operation voltage of $\sim 3.8 \text{ V}$ (vs. K^+/K) at C/20 ($1C = 116 \text{ mA h g}^{-1}$), corresponding to $\sim 1 \text{ mol } K^+$ de/intercalation in the structure. Moreover, at 5C, $K_{1.5}VOPO_4F_{0.5}$ retained $\sim 79\%$ of the capacity at C/20. Even after 300 cycles at 1C, $K_{1.5}VOPO_4F_{0.5}$ exhibited outstanding capacity retention of $\sim 86\%$ compared with the initial capacity, despite repeated de/intercalation of K^+ with large ionic size. These results demonstrate the high power-capability and excellent cycle performance of $K_{1.5}VOPO_4F_{0.5}$, which stem from its structural advantages. In addition, the reaction mechanism of $K_xVOPO_4F_{0.5}$ during K^+ de/intercalation was confirmed, including the single-phase reaction and V^{4+}/V^{5+} redox reaction, *via* first-principles calculation, *operando* XRD, and X-ray absorption near edge structure (XANES) spectroscopy.

Results and discussion

Preparation and characterization of $K_xVOPO_4F_{0.5}$

Because of difficulties involved with the direct synthesis of $K_xVOPO_4F_{0.5}$ using the conventional solid-state method, the electrochemical ion-exchange method was applied. As shown in Fig. S9,† preparation of $K_xVOPO_4F_{0.5}$ *via* the solid-state method using the stoichiometric elemental ratio resulted in the appearance of various impurities and second phases rather than the pure $K_xVOPO_4F_{0.5}$ phase.^{22–24} Further synthesis attempts of $K_xVOPO_4F_{0.5}$ using other methods are described in the ESI.† To obtain the highly pure $K_xVOPO_4F_{0.5}$ phase, we first prepared phase-pure $Na_{1.5}VOPO_4F_{0.5}$ powder using the solid-state method (Fig. S10†), and then, electrochemical ion exchange from Na^+ to K^+ was performed in the KIB system for 30 cycles (Fig. S11†). In addition, Fig. S12 and Table S3† presents the crystal structure and detailed structural information of $Na_{1.5}VOPO_4F_{0.5}$.

The initial charge capacity of $Na_{1.5}VOPO_4F_{0.5}$ in the KIB system was $\sim 121 \text{ mA h g}^{-1}$, corresponding to $\sim 0.93 \text{ mol } Na^+$ deintercalation. Because of the difficulty of further oxidation from V^{5+} to V^{6+} in the available voltage range, up to $\sim 1 \text{ mol } Na^+$ in $Na_{1.5}VOPO_4F_{0.5}$ could be deintercalated during the initial charge, which implies the occurrence of partial Na^+/K^+ ion exchange during the initial cycle. The remainder of the Na^+ in $K_xNa_{1.5-x}VOPO_4F_{0.5}$ was gradually exchanged to K^+ during subsequent cycles in the KIB system, which is consistent with the changed charge/discharge profiles depending on the degree of Na^+/K^+ ion exchange. The XRD patterns of $Na_{1.5}VOPO_4F_{0.5}$ and $K_xVOPO_4F_{0.5}$ are compared in Fig. S13,† showing the overall shifted XRD peaks and changed ratio of the peak intensities with the well retained crystal structure after the ion exchange, confirming the successful preparation of the $K_xVOPO_4F_{0.5}$ phase. In addition, it was confirmed that the reversible ion-exchange from K to Na ions also possible in $K_xVOPO_4F_{0.5}$ structure (ESI†).

The structural information and phase purity of the $K_xVOPO_4F_{0.5}$ phase were investigated by performing Rietveld refinement based on the XRD pattern. It was expected that structural information of the ion-exchanged $K_xVOPO_4F_{0.5}$ phase would be well consistent with that of pristine $Na_{1.5}VOPO_4F_{0.5}$ except difference of lattice parameters and existence of K instead of Na, if the Na ions in the pristine $Na_{1.5}VOPO_4F_{0.5}$ structure were successfully exchanged to K ions. As shown in

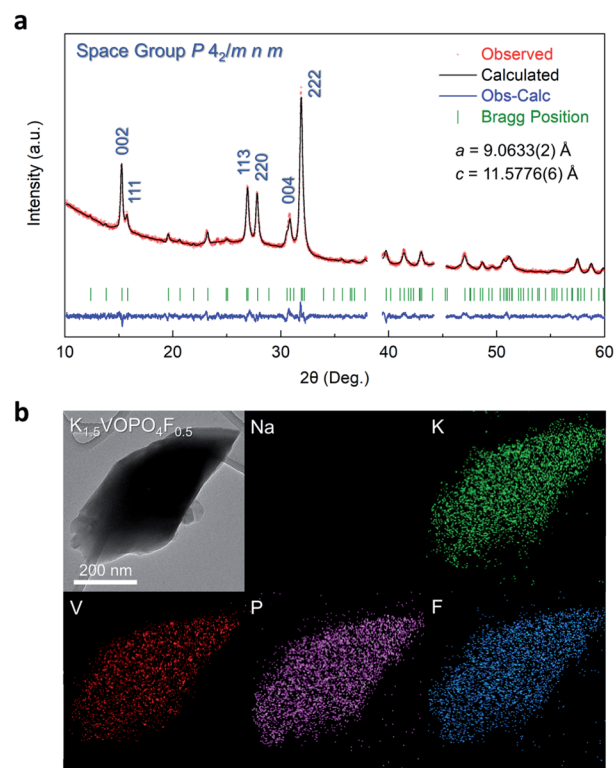


Fig. 1 (a) Refined XRD pattern of $K_{1.5}VOPO_4F_{0.5}$ using Rietveld refinement ($R_p = 3.56\%$, $R_{wp} = 4.87\%$, $R_1 = 5.61\%$, $R_F = 4.75\%$, and $\chi^2 = 2.73\%$). (b) TEM images and the corresponding EDS-mapping of $K_{1.5}VOPO_4F_{0.5}$ particle.

Fig. 1a, the lattice parameters of the $K_xVOPO_4F_{0.5}$ phase were $a = 9.0633(2) \text{ \AA}$, $c = 11.5776(6) \text{ \AA}$ with space group $P 4_2/mnm$ (tetragonal, #136). The high accuracy of the Rietveld refinement results was confirmed by the low reliability factors ($R_p = 3.56\%$, $R_{wp} = 4.87\%$, $R_1 = 5.61\%$, $R_F = 4.75\%$, and $\chi^2 = 2.73\%$). In addition, as shown in Table S4,[†] the lattice parameters of $K_xVOPO_4F_{0.5}$ were larger than those $Na_{1.5}VOPO_4F_{0.5}$ owing to the larger ionic size of K^+ (1.38 Å) than Na^+ (1.02 Å). Additional detailed structural information on $K_xVOPO_4F_{0.5}$, including the atomic positions, thermal factor, and occupancies, is presented in Table S5.[†] In addition, the elemental ratio in $K_xVOPO_4F_{0.5}$ was confirmed by inductively coupled plasma (ICP) spectroscopy analyses, which showed that the elemental ratio of K, V, and P in $K_xVOPO_4F_{0.5}$ is $\sim 1.5 : 1 : 1$. This elemental ratio was further confirmed by transmission electron microscopy-energy-dispersive X-ray spectroscopy (TEMEDS) analyses. Fig. 1b shows

that the K, V, P, and F elements were homogeneously distributed in $K_{1.5}VOPO_4F_{0.5}$ with a particle size of $\sim 500 \text{ nm}$, with no Na element signals detected. Moreover, in addition to the presence of K and not Na in the particle, the particle size and elemental ratio of V, P and F elements were similar to those of $Na_{1.5}VOPO_4F_{0.5}$ (Fig. S14[†]). The high similarity of the particle size and morphologies for $K_{1.5}VOPO_4F_{0.5}$ and $Na_{1.5}VOPO_4F_{0.5}$ was also confirmed by scanning electron microscopy (SEM) analysis (Fig. S15[†]). In addition, XANES analysis showed that the oxidation state of V ions in $K_{1.5}VOPO_4F_{0.5}$ was similar to that of $Na_{1.5}VOPO_4F_{0.5}$ and VO_2 (Fig. S16[†]). These experimental results based on XRD, TEM, SEM, and XANES analyses indicate that $K_{1.5}VOPO_4F_{0.5}$ was successfully obtained after the electrochemical Na^+/K^+ ion-exchange process from $Na_{1.5}VOPO_4F_{0.5}$.

As illustrated in Fig. 2a, the crystal structure of $K_{1.5}VOPO_4F_{0.5}$ consists of $[V_2O_{10}F]$ bi-octahedra and $[PO_4]$ tetrahedra that are

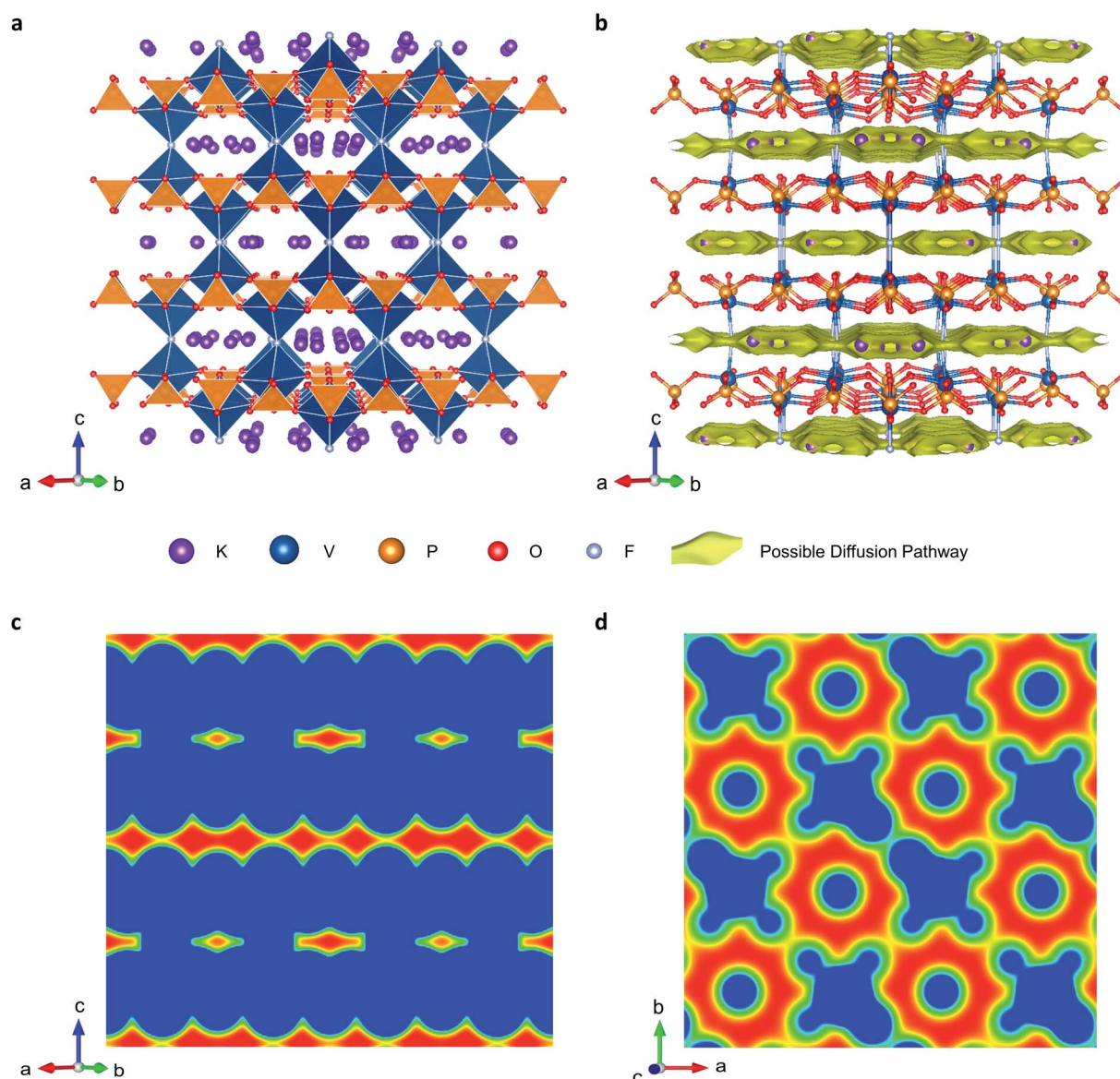


Fig. 2 (a) Crystal structure of $K_{1.5}VOPO_4F_{0.5}$. (b) 3D BVEL analysis of $K_{1.5}VOPO_4F_{0.5}$ with all possible K-ion positions and diffusion pathways. (c and d) 2D BVEL analysis of $K_{1.5}VOPO_4F_{0.5}$.

three-dimensionally interconnected with point sharing. In addition, the V–F bonding distance in the $[V_2O_{10}F]$ bi-octahedra is longer than the V–O bonding distance because of the stronger electronegativity of fluorine than oxygen. Based on the structural data collected from the Rietveld refinement, we performed BVEL analyses to predict the possible ionic diffusion pathways and atomic sites for K ions in the structure using the *Bond_str* program in the FullProf package.²⁵ The three-dimensional (Fig. 2b) and two-dimensional (Fig. 2c and d) views of the BVEL reveal that there are sufficiently large spaces for facile K^+ diffusion along the *ab* plane in the crystal structure, which can result in the outstanding power-capability of $K_{1.5}VOPO_4F_{0.5}$ as a promising cathode for KIBs. Moreover, it was verified that there are two K atomic sites in the $K_{1.5}VOPO_4F_{0.5}$ structure with

Wyckoff positions and atomic coordinates (*x*, *y*, *z*) of 8i (0.3327, 0.5580, 0) and 8i (0.0315, 0.7161, 0), confirming that the presence of ~ 1.5 mol K^+ in the $K_xVOPO_4F_{0.5}$ structure is reasonable.

Electrochemistry of $K_xVOPO_4F_{0.5}$

To predict the theoretical electrochemical properties of $K_{1.5}VOPO_4F_{0.5}$ in the KIB system, first-principles calculations were performed. Various K^+ /vacancy configurations of each $K_xVOPO_4F_{0.5}$ ($0 \leq x \leq 2$) phase were prepared using the cluster-assisted statistical mechanics (CASM) software.²⁶ Then, the formation energies of all the configurations were predicted and arranged in the form of a convex-hull plot (Fig. 3a). The convex hull plot is based on the relative formation energies of various $K_xVOPO_4F_{0.5}$ phases using total formation energies of

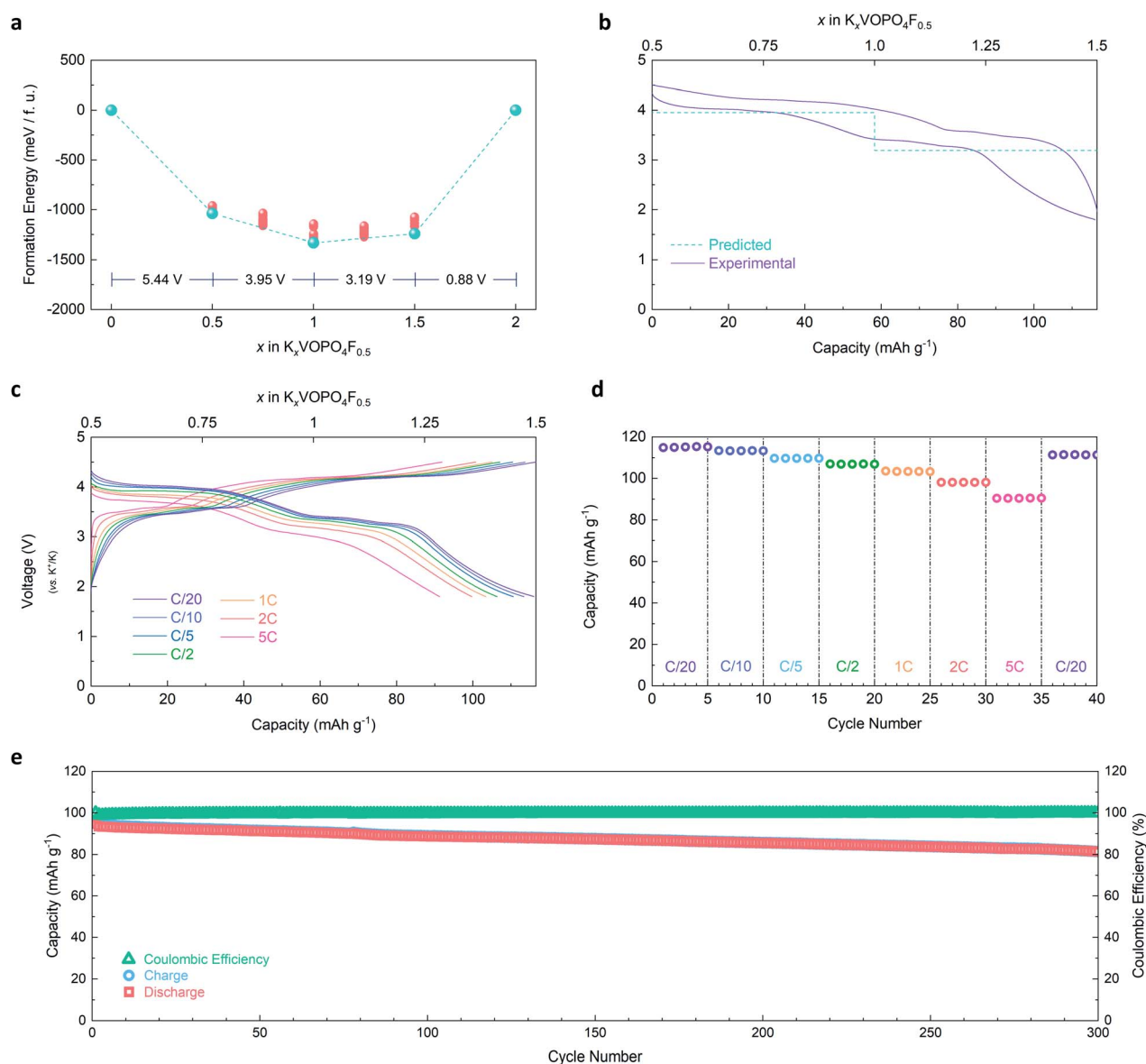


Fig. 3 (a) Formation energy with derived theoretical voltage of $K_xVOPO_4F_{0.5}$ ($0 \leq x \leq 2$). (b) Comparison of theoretical voltage prediction and experimental results for $K_xVOPO_4F_{0.5}$ ($0.5 \leq x \leq 1.5$). (c) Charge/discharge curves of $K_{1.5}VOPO_4F_{0.5}$ in the voltage range of 1.8–4.5 V at various discharge current rates. (d) Power-capability of $K_{1.5}VOPO_4F_{0.5}$. (e) Cycling performance of $K_{1.5}VOPO_4F_{0.5}$ over 300 cycles at 1C.

$K_0VOPO_4F_{0.5}$ and $K_2VOPO_4F_{0.5}$ compositions as reference, which more easily show not only existence of stable intermittent phases between end compositions but also energy difference between two phases relating to redox potentials, compared to the original plot based on the real formation energies.^{27,28} The relative formation energy was derived using the following equation;

$$E_{for} = E(K_xVOPO_4F_{0.5}) - \frac{(2-x)E(K_0VOPO_4F_{0.5}) + xE(K_2VOPO_4F_{0.5})}{2}$$

where E is the predicted formation energy for the most stable configuration of each component. The theoretical redox potentials of $K_xVOPO_4F_{0.5}$ were then derived using the following equation;

$$V = -\frac{E(K_{x_2}VOPO_4F_{0.5}) - E(K_{x_1}VOPO_4F_{0.5}) - (x_2 - x_1)E(K)}{(x_2 - x_1)F}$$

where V is the average redox potential in the compositional range between x_1 and x_2 , and F is the Faraday constant. It was predicted that ~ 1 mol K^+ can be reversibly de/intercalated in the $K_xVOPO_4F_{0.5}$ structure in the available voltage ranges. Fig. 3b demonstrates that these theoretical redox potentials of $K_xVOPO_4F_{0.5}$ ($0.5 \leq x \leq 1.5$) are consistent with its experimentally measured charge/discharge profile measured at the current rate of $C/20$ ($1C = 116 \text{ mA g}^{-1}$).

Electrochemical characterization of $K_{1.5}VOPO_4F_{0.5}$ was performed in the KIB system using K metal as the counter electrode and 0.5 M KPF_6 in ethylene carbonate (EC): propylene carbonate (PC) (volume ratio of 1 : 1) as the electrolyte. As shown in Fig. 3c and d, it was verified that $K_{1.5}VOPO_4F_{0.5}$ delivers a specific capacity of $\sim 116 \text{ mA h g}^{-1}$ at $C/20$ in the voltage range of 1.8–4.5 V (vs. K^+/K), corresponding to ~ 1 mol K^+ de/intercalation. Moreover, even at 5C, the specific capacity was maintained up to $\sim 91 \text{ mA h g}^{-1}$, which corresponds to $\sim 79\%$ of the capacity measured at $C/20$. Furthermore, $K_{1.5}VOPO_4F_{0.5}$ exhibited excellent cycle performance, with $\sim 86\%$ retention of the initial capacity after 300 cycles at 1C with a high coulombic efficiency of over $\sim 99\%$ (Fig. 3e). In addition, the outstanding power-capability of $K_{1.5}VOPO_4F_{0.5}$ in the KIB system was confirmed using the nudged elastic band (NEB) method based on first-principles calculation. The theoretical K^+ diffusion motion in the $K_xVOPO_4F_{0.5}$ structure and the theoretical activation barrier energy required for K^+ diffusion are shown in Fig. 4a and b. The activation barrier energy of $K_xVOPO_4F_{0.5}$ was predicted to be only $\sim 356 \text{ meV}$ along the K_1 – K_3 pathway, which implies facile K^+ diffusion along large two-dimensional pathways in $K_xVOPO_4F_{0.5}$ despite the large K^+ ionic radius. The competitiveness of $K_{1.5}VOPO_4F_{0.5}$ as a promising cathode for KIBs is also demonstrated through comparison with the electrochemical properties of reported cathode materials for KIBs, such as layered oxides, polyanionic compounds, and Prussian-blue analogues. As shown in Fig. 5, $K_{1.5}VOPO_4F_{0.5}$ delivers an energy density of $\sim 345.8 \text{ Wh kg}^{-1}$ at a power density of 2204 W kg^{-1} , which is larger than that of other cathode materials for KIBs. In addition, we performed a full-cell test of $K_{1.5}VOPO_4F_{0.5}$ using hard carbon as the anode. Fig. S17† shows that the full

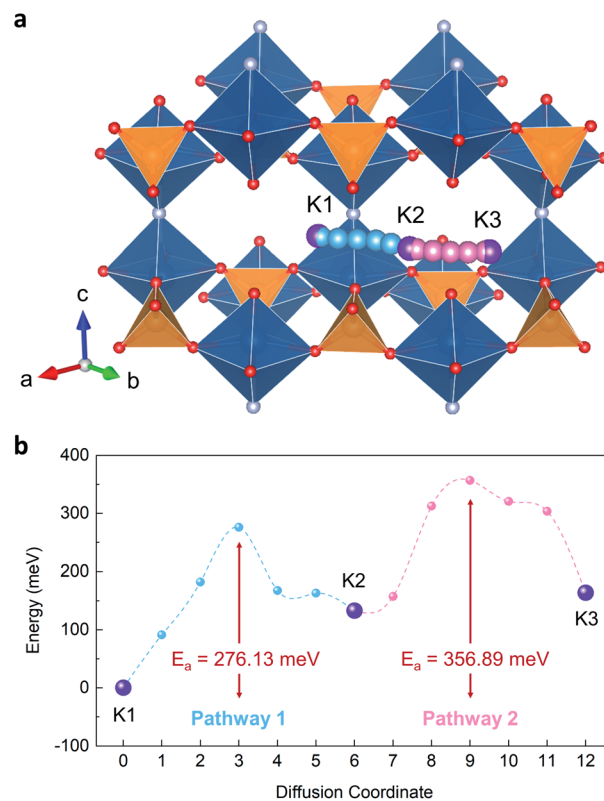


Fig. 4 (a) Diffusion pathways for K ions with (b) energy landscape determined using NEB method in $K_{1.5}VOPO_4F_{0.5}$ structure.

cell delivered an initial specific capacity of $\sim 92 \text{ mA h g}^{-1}$ at a current density of 116 mA g^{-1} and outstanding cyclability with capacity retention of $\sim 84\%$ compared with the initial capacity for 300 cycles, which indicates that $K_{1.5}VOPO_4F_{0.5}$ can be applied as a cathode for practical KIBs.

Structural change and reaction mechanism of $K_xVOPO_4F_{0.5}$ under K^+ de/intercalation

It was supposed that the remarkable cycle performance of $K_{1.5}VOPO_4F_{0.5}$ in the KIB system may originate from its stably well-retained crystal framework despite the repeated K^+ de/

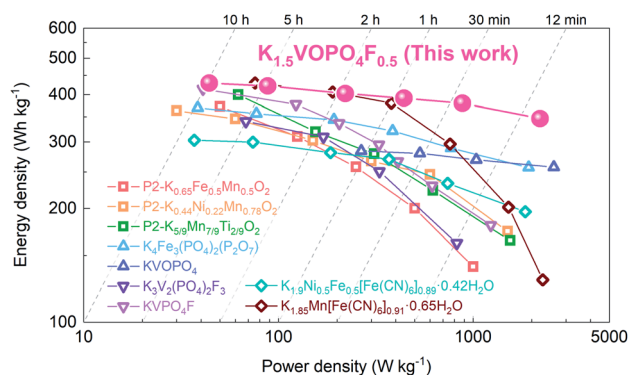


Fig. 5 Ragone plot of $K_{1.5}VOPO_4F_{0.5}$ and other cathode materials for KIBs.

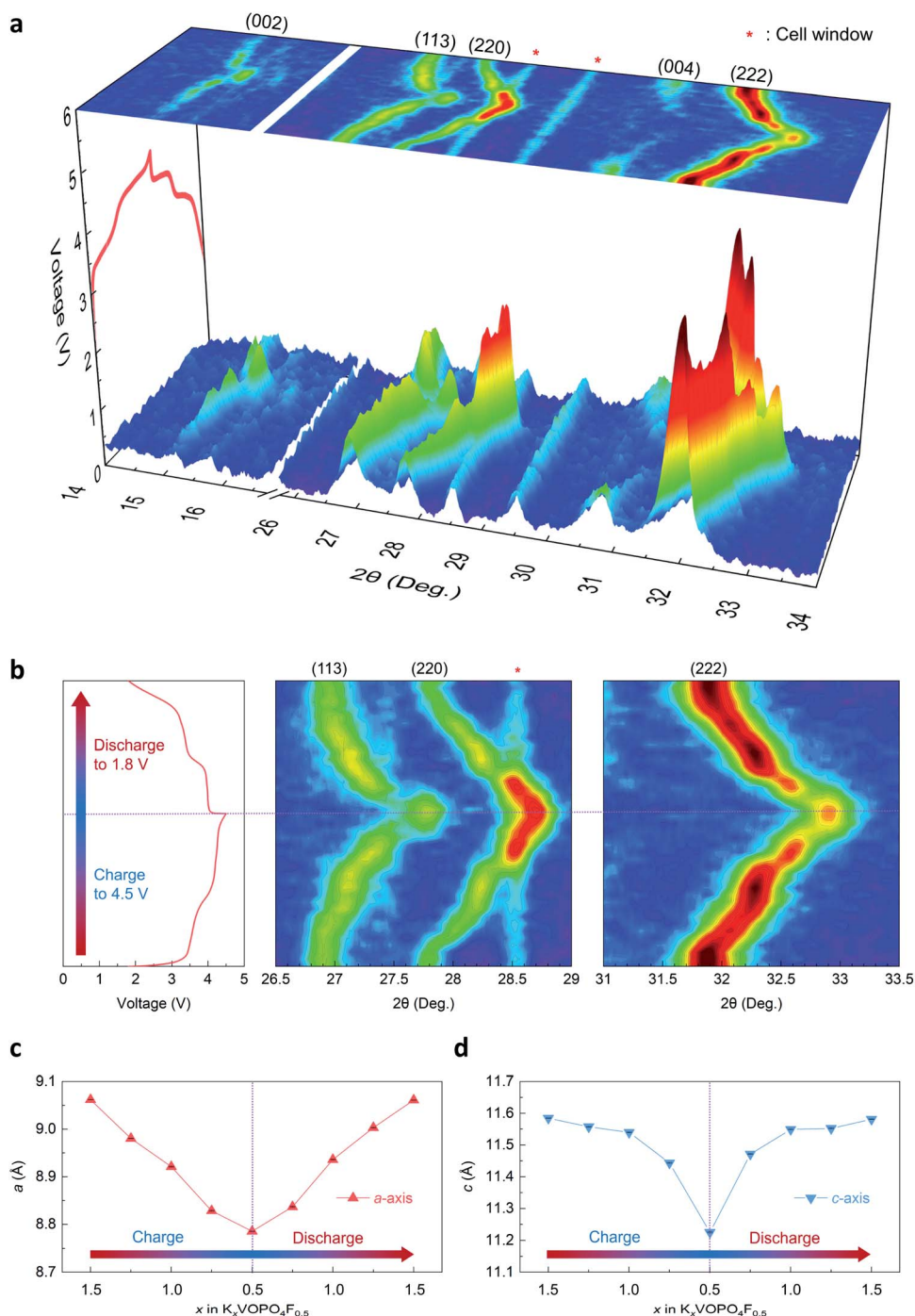


Fig. 6 (a) *Operando* XRD patterns of $K_xVOPO_4F_{0.5}$ ($0.5 \leq x \leq 1.5$) during charge/discharge. (b) Magnified view of *operando* XRD patterns with charge/discharge curves of $K_xVOPO_4F_{0.5}$ ($0.5 \leq x \leq 1.5$). (c and d) Change in (c) a and (d) c lattice parameters as a function of K content in $K_xVOPO_4F_{0.5}$ ($0.5 \leq x \leq 1.5$) verified through Rietveld refinement.

intercalation. To investigate the structural change as a function of K content in the $K_{1.5}VOPO_4F_{0.5}$ structure, *operando* XRD analysis was performed (Fig. 6a and b). The full *operando* XRD patterns are presented in Fig. S18.† The XRD peaks of $K_{1.5}VOPO_4F_{0.5}$, including those corresponding to the (113) and (222) planes, monotonously shifted toward higher/lower 2θ angle during charge/discharge. Furthermore, none of new peaks were observed, which means the occurrence of single-

phase reaction for $K_xVOPO_4F_{0.5}$ during K^+ de/intercalation. The change in the a and c lattice parameters of $K_{1.5}VOPO_4F_{0.5}$ during charge/discharge was analyzed using Rietveld refinement of the *operando* XRD patterns. As shown in Fig. 6c and d, the difference in the lattice parameters of $K_{1.5}VOPO_4F_{0.5}$ and $K_{0.5}VOPO_4F_{0.5}$ was determined to be only $\sim 4\%$, despite ~ 1 mol K^+ de/intercalation from/into the structure. Moreover, we investigated the changes in the morphology and crystal

structure of $K_{1.5}VOPO_4F_{0.5}$ after long-term cycling using *ex situ* SEM and XRD analyses. Fig. S19 and S20† show that no remarkable cracks or severe structural degradation were discovered in the $K_{1.5}VOPO_4F_{0.5}$ particles even after 300 cycles. These *operando* XRD and *ex situ* SEM and XRD results indicate that the high structural stability of $K_{1.5}VOPO_4F_{0.5}$ based on a three-dimensionally interconnected framework enables its long cycle-life in the KIB system.

In addition, *ex situ* X-ray absorption spectroscopy (XAS) analyses were performed to determine the redox reaction of vanadium ions during K^+ de/intercalation in the $K_xVOPO_4F_{0.5}$ structure. Fig. 7a shows that the V K-edge XANES spectrum of $K_xVOPO_4F_{0.5}$ shifted toward higher/lower energy level during charge/discharge, which indicates the occurrence of a reversible V^{4+}/V^{5+} redox reaction. These XANES results were also confirmed through first-principles calculation. As shown in

Fig. 7b, the theoretical integrated spin moments of V ions of $K_{1.5}V^{(4+)}OPO_4F_{0.5}$ and $K_{0.5}V^{(5+)}OPO_4F_{0.5}$ were predicted to be +1 and 0, respectively, which implies the occurrence of the V^{4+}/V^{5+} redox reaction during K^+ deintercalation from $K_{1.5}VOPO_4F_{0.5}$. Moreover, the local structural change of $K_xVOPO_4F_{0.5}$ during K^+ de/intercalation was investigated using *ex situ* extended X-ray absorption fine structure (EXAFS) analyses. Fig. 7c shows that the V–O and V–F bonding distances of $[VO_5F]$ octahedra in $K_xVOPO_4F_{0.5}$ slightly decreased with the redox reaction from V^{4+} to V^{5+} during K^+ deintercalation from the structure. To calculate accurate V–O and V–F bond distances, we performed fitting processes on the *ex situ* EXAFS spectrum of $K_xVOPO_4F_{0.5}$ under k^3 -weight conditions in the fitting range of 1.15–2.5 Å for the first shell, corresponding to the V–O and V–F bonds. The amplitude reduction factor S_0^2 was set to 0.9. Fig. 7d shows that the average V–O and V–F bonding distances decreased from

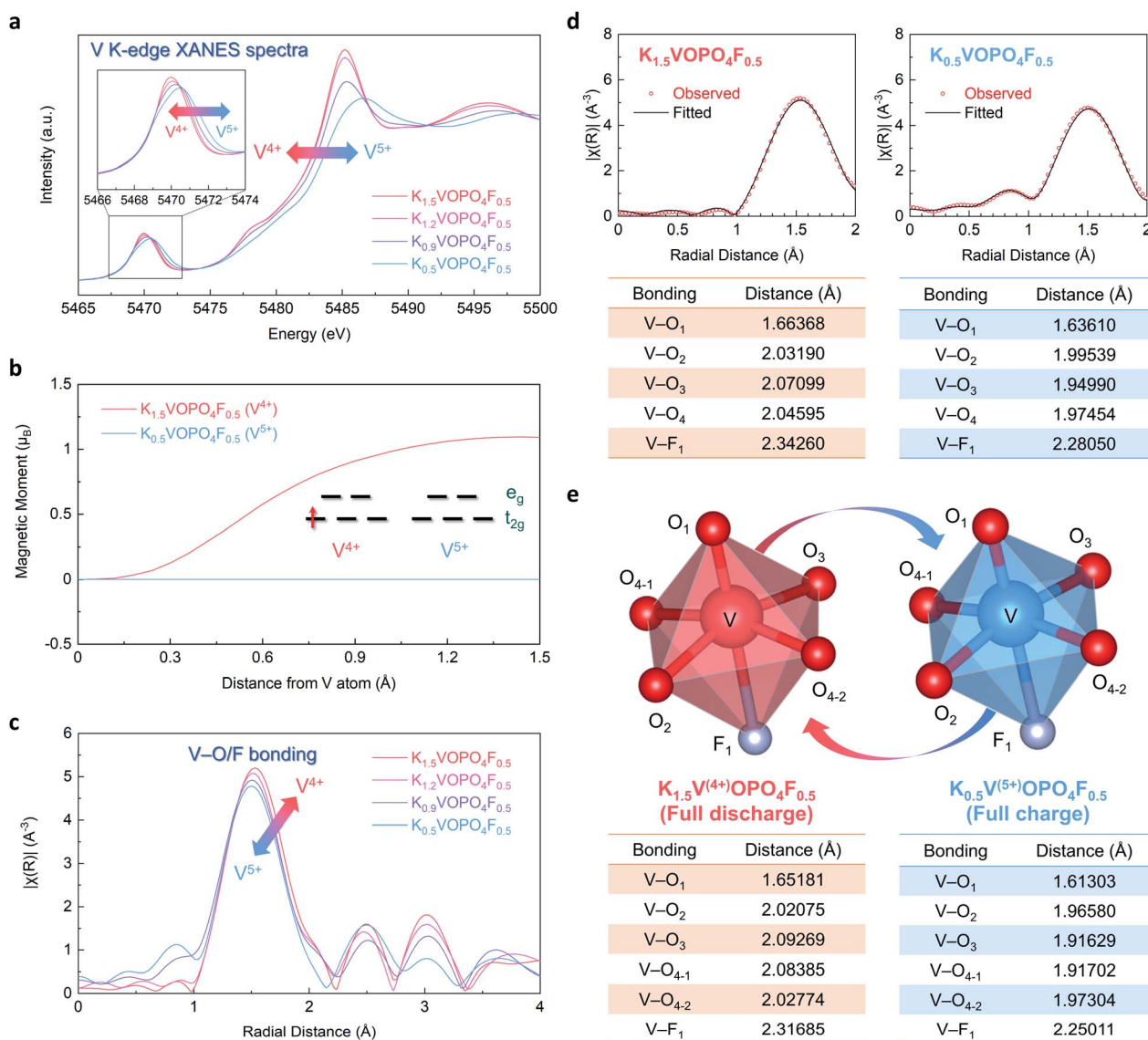


Fig. 7 (a) V K-edge XANES spectrum of $K_xVOPO_4F_{0.5}$ ($0.5 \leq x \leq 1.5$). (b) Integrated spin moments of $K_{1.5}VOPO_4F_{0.5}$ and $K_{0.5}VOPO_4F_{0.5}$. (c) EXAFS spectra of $K_xVOPO_4F_{0.5}$ ($0.5 \leq x \leq 1.5$). (d) EXAFS fits to data of $K_{1.5}VOPO_4F_{0.5}$ and $K_{0.5}VOPO_4F_{0.5}$. (e) V–O and V–F bonding distances of VO_5F octahedra in $K_{1.5}VOPO_4F_{0.5}$ and $K_{0.5}VOPO_4F_{0.5}$ structure verified through first-principles calculation.

~ 1.971 to ~ 1.906 Å and from ~ 2.342 to ~ 2.280 Å, respectively, during K^+ deintercalation, which is consistent with the first-principles calculation results predicting the local environment of $[VO_5F]$ octahedra in $K_{1.5}V^{(4+)}OPO_4F_{0.5}$ and $K_{0.5}V^{(5+)}OPO_4F_{0.5}$ (Fig. 7e).

Conclusions

We successfully prepared $K_{1.5}VOPO_4F_{0.5}$, a promising cathode material for KIBs, using an electrochemical ion-exchange process. The $[V_2O_{10}F]$ bi-octahedra and $[PO_4]$ tetrahedra, three-dimensionally interconnected in the $K_{1.5}VOPO_4F_{0.5}$ crystal structure, provide a robust structural framework contributing to the facile K^+ diffusion despite the large ionic radius of K^+ ions. Through first-principles calculations, the theoretical characteristics of $K_{1.5}VOPO_4F_{0.5}$, including the available voltage range, total molar number of storable K^+ ions per formula unit, and activation barrier energy, were confirmed. $K_{1.5}VOPO_4F_{0.5}$ delivered a specific capacity of ~ 116 mA h g^{-1} , which corresponds to ~ 1 mol of K ions based on the V^{4+}/V^{5+} redox reaction with high operation voltage of ~ 3.8 V. In particular, $K_{1.5}VOPO_4F_{0.5}$ exhibited a remarkably low activation barrier energy, which is related to the outstanding power-capability at 5C, maintaining $\sim 79\%$ of the measured capacity at C/20. Furthermore, it was demonstrated that the outstanding long-term cycle life of $K_{1.5}VOPO_4F_{0.5}$ with $\sim 86\%$ capacity retention for 300 cycles results from not only the small structural change during K^+ de/intercalation but also the stably retained crystal structure despite repeated charge/discharge cycles. We believe that our findings will be useful in the development of new cathode materials with excellent electrochemical properties for KIBs and other alkali-ion-based rechargeable battery systems.

Experimental

Preparation of $Na_{1.5}VOPO_4F_{0.5}$

Before the synthesis of $Na_{1.5}VOPO_4F_{0.5}$, $VOPO_4$ was first synthesized as a precursor. V_2O_5 and $NH_4H_2PO_4$ were stoichiometrically mixed using a conventional ball-milling machine at 300 rpm for 24 h under an air atmosphere. The mixed powder was pelletized and heated at 750 °C for 4 h (heating rate of 5 °C min^{-1}) in air to obtain the yellow-colored $VOPO_4$. Then, $VOPO_4$, NaF (Alfa Aesar, 99%), and Na_2CO_3 (Sigma Aldrich, 99.5%) were stoichiometrically mixed using the high-energy ball-milling machine at 300 rpm for 24 h under an Ar atmosphere. The mixed powder was pelletized and heated at 750 °C for 30 min (heating rate of 2.5 °C min^{-1}) in Ar condition to obtain the green-colored $Na_{1.5}VOPO_4F_{0.5}$. To enhance the conductivity, the $Na_{1.5}VOPO_4F_{0.5}$ powder was carbon-coated with Super-P (conducting carbon) in a weight ratio of 85 : 15 using conventional ball-milling at 300 rpm for 12 h under an air atmosphere.

Electrochemical characterization

The $Na_{1.5}VOPO_4F_{0.5}$ electrode was prepared by mixing the active material, Super-P, and poly(vinylidene fluoride) (PVDF; binder) using *N*-methyl-2-pyrrolidone (NMP) as the solvent. The total composition of the electrode was adjusted to 70 wt% active materials, 20 wt% Super-P, and 10 wt% PVDF. A slurry of the mixture was applied to Al foil using a doctor blade. The electrode was dried at 80 °C for 12 h to evaporate the NMP. The mass loading of the electrode was ~ 2 mg cm^{-2} . The Na^+ storage performance of $Na_{1.5}VOPO_4F_{0.5}$ is provided in ESL†

R2032-type coin cells were prepared using the $Na_{1.5}VOPO_4F_{0.5}/K_{1.5}VOPO_4F_{0.5}$ electrode, K metal as the reference/counter electrode, a separator (Whatman GF/F glass fiber), and 0.5 M KPF₆ in ethylene carbonate (EC):propylene carbonate (PC) (volume ratio of 1 : 1) as the electrolyte. The coin cells were assembled in an Ar-filled glove box.

Galvanostatic charge/discharge tests were performed at various current rates (C/20, C/10, C/5, C/2, 1C, 2C, and 5C in the voltage range of 1.8–4.5 V) using a battery test system (WonA-Tech WBCS3000). In this experiment, 1C corresponds to ~ 116 mA g^{-1} .

Electrochemical ion-exchange process for $K_{1.5}VOPO_4F_{0.5}$

To prepare the $K_{1.5}VOPO_4F_{0.5}$, the $Na_{1.5}VOPO_4F_{0.5}$ electrode was assembled into a K-ion cell, and Na ions in the $Na_{1.5}VOPO_4F_{0.5}$ were deintercalated by charging to 4.5 V. After the deintercalation of Na ions, the cell was subsequently cycled 30 times in the voltage range of 1.8–4.5 V to remove the residual Na ions. At the cut-off voltages lower than 4.5 V, Na ions in $Na_{1.5}VOPO_4F_{0.5}$ structure was not completely deintercalated (see ESL†).

Fabrication of full-cell

The full cells were fabricated using commercial hard carbon (Kureha) as the anode. The hard carbon was heated at 1000 °C for 2 h (heating rate of 2.5 °C min^{-1}) in Ar to remove residual water and air-oxidized substances on the surface of the hard carbon particles. The hard carbon electrode was fabricated in the same way using the same ratio as the $Na_{1.5}VOPO_4F_{0.5}$ electrode except that Cu foil was used. To minimize the irreversibility of hard carbon, the hard carbon electrode was pre-cycled as a half-cell through direct contact with K metal in the voltage range of 0.01–2.0 V. Then, R2032-type full-cells were assembled with the $K_{1.5}VOPO_4F_{0.5}$ cathode and hard carbon anode (capacity ratio of negative and positive electrodes adjusted to be ~ 1.2) in an Ar-filled glove box. The detailed properties of hard carbon, such as electrochemical performance and heat-treatment effects are described in ESL†

Materials characterization

$K_{1.5}VOPO_4F_{0.5}$ and $Na_{1.5}VOPO_4F_{0.5}$ were analyzed using XRD (Malvern Panalytical Empyrean) with Cu $K\alpha$ radiation ($\lambda = 1.54178$ Å). The step size was 0.013°, and the 2θ range of 10° to 60° was examined. Rietveld refinement of the XRD data was performed using FullProf software.²⁹ The morphology and

particle size of $K_{1.5}VOPO_4F_{0.5}$ and $Na_{1.5}VOPO_4F_{0.5}$ were determined using scanning electron microscopy (SEM; Hitachi SU-8010) and field-emission transmission electron microscopy (FE-TEM; JEOL JEM-F200; installed at the National Center for Inter-university Research Facilities (NCIRF) at Seoul National University). The atomic ratios of elements such as Na, K, V, and P were determined using inductively coupled plasma-optical emission spectrometry (ICP-OES). V K-edge X-ray absorption spectroscopy (XAS) spectra were obtained at beamline 10C at the Pohang Accelerator Laboratory (PAL). The *operando* XRD patterns of $K_{1.5}VOPO_4F_{0.5}$ were analyzed using XRD (PANalytical, Empyrean) with Cu $K\alpha$ radiation ($\lambda = 1.54178 \text{ \AA}$). The step size was 0.026° , and the 2θ range of 10° to 40° was examined.

Computational details

All the density functional theory (DFT) calculations were performed using the Vienna *Ab initio* Simulation Package (VASP).³⁰ We used projector-augmented wave (PAW) pseudopotentials³¹ with a plane-wave basis set as implemented in VASP. Perdew–Burke–Ernzerhof (PBE) parametrization of the generalized gradient approximation (GGA)³² was used for the exchange–correlation functional. For the DFT calculations, a $3 \times 3 \times 3$ k -point grid was used to calculate a $1 \times 1 \times 1$ supercell structure of $K_{1.5}VOPO_4F_{0.5}$. The GGA + U method³³ was adopted to address the localization of the d-orbital in V ions, with a U value of 4.2 eV, as used in previous studies.^{34–36} A kinetic energy cutoff of 500 eV was used in all the calculations, and all the structures were optimized until the force in the unit cell converged to within 0.05 eV \AA^{-1} .

CASM software²⁶ was used to generate all the K^+ /vacancy configurations for each composition, followed by full DFT calculations on a maximum of 20 configurations with the lowest electrostatic energy for each composition used to obtain the convex hull plot of $K_{1.5}VOPO_4F_{0.5}$.

NEB calculations³⁷ were performed to determine the activation barrier for K^+ diffusion in the $K_{1.5}VOPO_4F_{0.5}$ structure. To perform the calculations, five intermediate images were generated between each K site. These structures were then calculated using the NEB algorithm with fixed lattice parameters and free internal atomic positions.

The schematic illustrations, crystal structure with BVOL, and NEB calculation results for K^+ diffusion pathways were drawn using VESTA software.³⁸

Conflicts of interest

There are no conflicts to declare.

Acknowledgements

This research was supported by the National Research Foundation of Korea funded by the Ministry of Science and ICT of Korea (NRF-2018K1A4A3A01064272, NRF-2020M2D8A2070870, NRF-2020M3H4A1A03084256 and NRF-2021R1A2C1014280).

Also, this work was supported by the Korea Institute of Materials Science (KIMS) of the Republic of Korea (PNK7330).

References

- 1 B. Dunn, H. Kamath and J.-M. Tarascon, *Science*, 2011, **334**, 928–935.
- 2 J. B. Goodenough, *Nature Electronics*, 2018, **1**, 204.
- 3 A. Konarov, S.-T. Myung and Y.-K. Sun, *ACS Energy Lett.*, 2017, **2**, 703–708.
- 4 N. Yabuuchi, M. Kajiyama, J. Iwatate, H. Nishikawa, S. Hitomi, R. Okuyama, R. Usui, Y. Yamada and S. Komaba, *Nat. Mater.*, 2012, **11**, 512–517.
- 5 J.-M. Tarascon and M. Armand, *Materials for Sustainable Energy*, 2010, **26**, 171–179.
- 6 K. Kang, Y. S. Meng, J. Bréger, C. P. Grey and G. Ceder, *Science*, 2006, **311**, 977–980.
- 7 Y. Tian, G. Zeng, A. Rutt, T. Shi, H. Kim, J. Wang, J. Koettgen, Y. Sun, B. Ouyang, T. Chen, Z. Lun, Z. Rong, K. Persson and G. Ceder, *Chem. Rev.*, 2021, **121**, 1623–1669.
- 8 S. W. Kim, D. H. Seo, X. Ma, G. Ceder and K. Kang, *Adv. Energy Mater.*, 2012, **2**, 710–721.
- 9 W. Zhang, Y. Liu and Z. Guo, *Sci. Adv.*, 2019, **5**, eaav7412.
- 10 J. Kang, W. Ko, H. Park, Y. Lee, J. H. Jo, J. U. Choi, S. T. Myung and J. Kim, *Energy Storage Materials*, 2020, **33**, 276–282.
- 11 Z. Jian, W. Luo and X. Ji, *J. Am. Chem. Soc.*, 2015, **137**, 11566–11569.
- 12 J.-Y. Hwang, J. Kim, T.-Y. Yu, H.-G. Jung, J. Kim, K.-H. Kim and Y.-K. Sun, *J. Mater. Chem. A*, 2019, **7**, 21362–21370.
- 13 J. U. Choi, J. Kim, J. H. Jo, H. J. Kim, Y. H. Jung, D.-C. Ahn, Y.-K. Sun and S.-T. Myung, *Energy Storage Materials*, 2020, **25**, 714–723.
- 14 J.-Y. Hwang, J. Kim, T.-Y. Yu, S.-T. Myung and Y.-K. Sun, *Energy Environ. Sci.*, 2018, **11**, 2821–2827.
- 15 H. Park, H. Kim, W. Ko, J. H. Jo, Y. Lee, J. Kang, I. Park, S.-T. Myung and J. Kim, *Energy Storage Materials*, 2020, **28**, 47–54.
- 16 B. C. Melot and J.-M. Tarascon, *Acc. Chem. Res.*, 2013, **46**, 1226–1238.
- 17 T. Hosaka, T. Shimamura, K. Kubota and S. Komaba, *Chem. Rec.*, 2019, **19**, 735–745.
- 18 X. Lin, J. Huang, H. Tan, J. Huang and B. Zhang, *Energy Storage Materials*, 2019, **16**, 97–101.
- 19 H. Kim, D. H. Seo, M. Bianchini, R. J. Clément, H. Kim, J. C. Kim, Y. Tian, T. Shi, W. S. Yoon and G. Ceder, *Adv. Energy Mater.*, 2018, **8**, 1–12.
- 20 N. Sharma, P. Serras, V. Palomares, H. E. A. Brand, J. Alonso, P. Kubiak, M. L. Fdez-Gubieda and T. Rojo, *Chem. Mater.*, 2014, **26**, 3391–3402.
- 21 Y.-U. Park, D.-H. Seo, H.-S. Kwon, B. Kim, J. Kim, H. Kim, I. Kim, H.-I. Yoo and K. Kang, *J. Am. Chem. Soc.*, 2013, **135**, 13870–13878.
- 22 H. Graetsch, *Acta Crystallogr., Sect. C: Cryst. Struct. Commun.*, 2000, **56**, 401–403.
- 23 F. Girgsdies, M. Schneider, A. Brückner, T. Ressler and R. Schlögl, *Solid State Sci.*, 2009, **11**, 1258–1264.

- 24 S. S. Fedotov, N. R. Khasanova, A. S. Samarin, O. A. Drozhzhin, D. Batuk, O. M. Karakulina, J. Hadermann, A. M. Abakumov and E. V. Antipov, *Chem. Mater.*, 2016, **28**, 411–415.
- 25 S. Adams, *Solid State Ionics*, 2000, **136–137**, 1351–1361.
- 26 A. Van der Ven, J. C. Thomas, Q. Xu and J. Bhattacharya, *Mathematics and Computers in Simulation*, 2010, **80**, 1393–1410.
- 27 S. Jana, S. Thomas, C. H. Lee, B. Jun and S. U. Lee, *J. Mater. Chem. A*, 2019, **7**, 12706–12712.
- 28 C. H. Lee and S. U. Lee, *J. Phys. Chem. C*, 2018, **122**, 15155–15162.
- 29 J. Rodríguez-Carvajal, *Commission on Powder Diffraction (IUCr) Newsletter*, 2001, **26**, 12–19.
- 30 G. Kresse and J. Furthmüller, *Comput. Mater. Sci.*, 1996, **6**, 15–50.
- 31 P. E. Blöchl, *Phys. Rev. B: Condens. Matter Mater. Phys.*, 1994, **50**, 17953–17979.
- 32 J. P. Perdew, K. Burke and M. Ernzerhof, *Phys. Rev. Lett.*, 1996, **77**, 3865–3868.
- 33 V. I. Anisimov, F. Aryasetiawan and A. I. Lichtenstein, *J. Phys.: Condens. Matter*, 1997, **9**, 767–808.
- 34 J. Kim, G. Yoon, H. Kim, Y.-U. Park and K. Kang, *Chem. Mater.*, 2018, **30**, 3683–3689.
- 35 S. Y. Lim, H. Kim, R. A. Shakoor, Y. Jung and J. W. Choi, *J. Electrochem. Soc.*, 2012, **159**, A1393–A1397.
- 36 W. Ko, J.-K. Yoo, H. Park, Y. Lee, I. Kang, J. Kang, J. H. Jo, J. U. Choi, J. Hong, S.-T. Myung and J. Kim, *Nano Energy*, 2020, **77**, 105175.
- 37 G. Henkelman, B. P. Uberuaga and H. Jónsson, *J. Chem. Phys.*, 2000, **113**, 9901–9904.
- 38 K. Momma and F. Izumi, *J. Appl. Crystallogr.*, 2008, **41**, 653–658.